Mobile evaporite enhances the cycle of physical−chemical erosion in badlands

Ci-Jian Yang[1,2], Pei-Hao Chen[1], Erica D. Erlanger[2], Jens M. Turowski[2], Sen Xu[2], Tse-Yang Teng[3], Jiun-Chuan Lin[1], Jr-Chuang Huang[1]

1. Department of Geography, National Taiwan University, No. 1, Sec. 4, Roosevelt Rd., Taipei 10617, Taiwan.
2. German Research Centre for Geosciences (GFZ), Telegrafenberg 14473, Potsdam, Germany.
3. Sustain-vision Consulting Co. Ltd., Taipei 11168, Taiwan.

Correspondence to: Ci-Jian Yang (d03228001@ntu.edu.tw)

Abstract. Chemical weathering driven by physical erosion is a natural process that strongly affects chemical and solid matter budgets at the Earth's surface. However, the influence of extreme climatic erosion on chemical weathering dynamics is poorly understood. Badland landscapes formed in highly erodible, homogeneous substrates have the potential to respond to individual events on scales that are rapid enough for direct observation. Here, we assess the geochemical and grain-size composition of suspended sediment and riverine chemistry measurements collected from two catchments during the 2017 Nesat and Haitang typhoons in southwestern Taiwan. During the typhoons, the Na^+ concentration covaried with suspended sediment concentration, which we attributed to sodium-induced deflocculation. Evaporite weathering at peak rainfall is succeeded by peak silicate weathering at maximum discharge, which dominates the weathering signal of the event. Overall, our observations suggest that initial weathering of near-surface evaporite enhances the physical erosion of silicate rock during extreme rainfall events.

1. Introduction

Chemical weathering induced by physical erosion controls nutrient supply to ecosystems (Milligan and Morel, 2002), reflects dynamic surface processes (e.g., Calmels et. al., 2011; Clift et. al., 2014; Emberson et. al., 2016; Meyer et. al., 2017), and regulates the global carbon cycle and the evolution of Earth's long-term climate (Berner et al., 1983; Ram et al., 1992; Gaillardet et al., 1999). In most landscapes, physical erosion and chemical weathering operate on geological timescales that may be difficult to observe on human timescales (e.g., Maher et al., 2014). However, in many landscapes erosion dominantly occurs during stochastic events, such as storms (e.g., Hartshorn et al., 2002; Lee et al., 2020; Wang et al., 2021). In particular, typhoons are able to transport large volumes of water and dissolved solids within hours to days, allowing us to observe the interactions between physical erosion and chemical weathering in landscapes impacted by them. Nevertheless, observations of the interaction between extreme physical erosion and chemical weathering dynamics are limited (Meyer et. al., 2017). Furthermore, the lack of high-frequency stream water sampling leads to a fundamental difficulty in constraining the dynamic behavior between physical erosion and chemical weathering during a high discharge period (e.g., a typhoon), which could have key implications for our ability to quantify topographic responses to these events.

Badlands are landscapes characterized by highly erodible and weathered substrates, that are largely devoid of vegetation. The high erodibility of these landscapes provides a unique opportunity to investigate and quantify denudation processes that operate at short timescales (Cheng et al., 2019; Yang et al, 2019, 2021a; 2021b). Badlands is typically dominated by mudstones and clays, and soils that contain clays saturated in sodium ions are particularly vulnerable to erosion by water. Sodium ions alter the layer charge of double-layered clay minerals (i.e. smectite) and cause the clays to deflocculate, which refers to the process of breaking up the clay (and ultimately the soil) into finer particles that are more easily washed away by water (e.g., Faulkner et al., 2004; Mitchell et al., 1993; Rengasamy and Olsson, 1991; Rengasamy et al.,1984; Sherard et al., 1976; Kašanin-Grubin et. al., 2018). Additionally,

48   mineral assemblage affects the stability of soil aggregates; for example, small amounts of smectite in

49   kaolinitic materials cause it to be more dispersive and unstable (Levy et al., 1993).

50

51   Previous studies in the badlands of southwestern (SW) Taiwan have revealed that halite and gypsum

52   dissolve at depth and migrate to the hillslope surface and deposit in desiccation cracks during the dry

53   season (Higuchi et al., 2013, 2015; Nakata and Chigira, 2009). Others have observed that pore waters

54   found in the near-surface mudstone have Na^+ concentrations of 1−3 million μmol/L at 1−2 cm depth

55   (Nakata and Chigira, 2009). Mud cracks lead to the properties of the mudstone, e.g., rock density,

56   water permeability, and ion concentration between the surface (a few centimeters to 10 cm depth) and

57   bedrock are different (Fig. S1). For example, the bedrock hardly participates in physical erosion during

58   a rainfall event due to low permeability. We hypothesize that the dissolved halite and gypsum re-

59   crystallize in the near-surface and are deposited in the mudstone cracks through capillary action during

60   the dry season. Subsequent precipitation dissolves the evaporite, and the dissolved Na^+ enhances

61   erosion by clay dispersity and exposes more weatherable materials, forming a positive feedback cycle.

62   Assuming a mudstone substrate that is primarily comprised of silicate minerals, we expect that

63   concentration of evaporite ions should be consistent with changes in the sediment concentration and

64   the concentration of silicate ions.

65

66   To investigate this potential feedback between evaporite dissolution and erosion, we use suspended

67   sediment concentrations (SSC) and stream chemistry data from two catchments in the badlands of SW

68   Taiwan (Fig. 1), collected at a temporal resolution of 3 hours over 3 days. We interpret our observations

69   in the badlands to reflect how the excess sodium that re-precipitates at surface in dry season enhances

70   physical erosion and chemical weathering in the following typhoon event.

71

72   **2. Geological and Meteorological Setting**

73 In Taiwan's badlands, the annual precipitation is about 2 m, and 90% of the rainfall is concentrated in

74 the rainy season. The rainy season lasts from May to October and reaches its peak in August, with over

75 400 mm of precipitation within a single month. In contrast, less than 40 mm of average monthly rainfall

76 is measured from November to April. We collected river water samples from two sites downstream of

77 the studied badland areas. The first site, Nanxiong Bridge (NX), is located at the midstream of the

78 Erren River and has a drainage area of 175 km^2. This area includes badlands covering an area of 4.37

79 km^2, which accounts for 2.49% of the total catchment area (Fig.1). The Erren River catchment is

80 predominantly underlain by Plio-Pleistocene mudstones, which are several kilometers thick, and

81 mainly feature illite (30.54%) and chlorite (28.70%) minerals (Tsai, 1984a). During the dry seasons,

82 the pore water chemistry in the near-surface mudstones is mainly composed of Na^+, Cl^-, Ca^{2+} and SO_4^{2-}

83 (Nakata and Chigira, 2009).

84

85 The gauging station at Nanxiong Bridge (NX) provides hourly discharge data for calculating sediment

86 and solute fluxes. The annual average discharge of Nanxiong Bridge station is 10.2 m^3/s, and the

87 typhoon season accounts for 84% of the total discharge. The meteorological station at Gutingkeng

88 (GTK) is located 5.5 km from Nanxiong Bridge and provides hourly precipitation data. Our second

89 sampling site is Guting (GT) Bridge, with an upstream drainage area of 79 km^2 and a badlands area of

90 1.87 km^2, corresponding to 2.37% of the total area. Guting Bridge is located adjacent to a badlands

91 conservation area, so the riverine water chemistry reflects the weathering products derived from the

92 adjacent hillslopes. Due to a lack of stream discharge observations at Guting Bridge, we use hourly

93 precipitation data at GTK, which is less than 1 km from the sampling site, to quantify the impact of

94 the typhoon events.

95
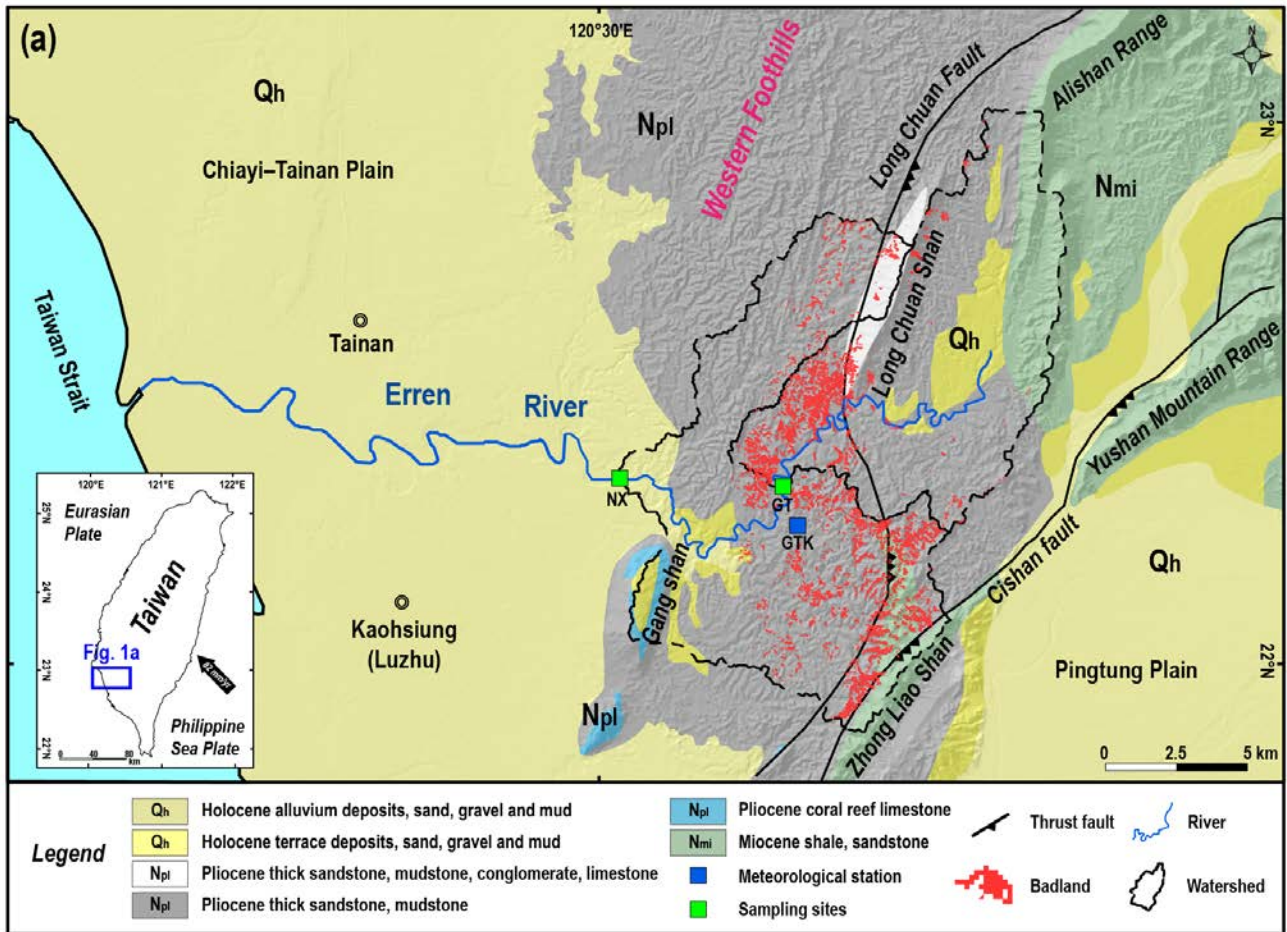
Figure 1. Location of sampling sites and geology of the study area. (a) The geological map of the study area (Source: Central Geological Survey, 2013). The green squares are sampling sites; hourly stream discharge data were obtained from the Nanxiong Bridge (NX) hydrometric station (Water Resources Agency). The blue square is the meteorological station, which provides hourly precipitation data (Central Weather Bureau, https://dbar.pccu.edu.tw/).

3. Methods and Materials

3.1 Water Sampling

We collected 42 stream samples from the two sampling sites for the typhoon period of July 2017. During sample collection, two 1000 ml PE bottles were dropped 1 to 2 meters below the water surface of the river simultaneously. Suspended sediment concentration (SSC) was subsequently calculated from the water collected in one of the PE bottles, and riverine chemistry was determined from water collected in the other bottle. Samples were filtered *in situ,* and the filtrate was preserved in the refrigerator for laboratory analysis. Additionally, 31 samples were collected from September 2014 to

111 December 2016 in the second half of every month at Nanxiong Bridge for non-typhoon periods, using

112 the same sampling procedure.

113

114 3.2 Dissolved load and sediment chemistry analysis

115 For the riverine dissolved load, we measured major dissolved anions (Cl^-, SO_4^{2-}, NO_2^-, NO_3^-, F^-) on an

116 Ion chromatography (IC, Metrohm Basic-883 plus), and we measured major dissolved cations (Na^+,

117 K^+, Mg^{2+}, Sr^{2+}, Ba^{2+}, Si^{4+}) on an ICP-OES (PerkinElmer, Optima 2100DV). We measured bulk

118 sediment chemistry from two samples of suspended sediment collected from Guting Bridge at low

119 flow before the typhoon event (2.26 m^3/s) and at the peak of runoff (724.32 m^3/s). About 0.7 g of dried

120 sediment sample was combusted in the muffle furnace at 650°C for 2 hours and then weighed to obtain

121 the loss on ignition (LOI). Afterward, an aliquot of ~100 mg from the residue was digested with a

122 mixture of concentrated HF and aqua regia. After digestion and drying, the sample was dissolved in

123 0.3 N HNO_3 for elemental determination. Major elemental concentrations of sediment samples were

124 obtained by ICP-OES (Varian 720-ES) at the GFZ German Research Centre for Geosciences.

125

126 **3.3 Grain size of suspended load**

127 Before measuring grain size, we removed the non-clastic deposition, i.e., sea salt, organic matter, and

128 carbonate. To remove sea salt, ~1 g of dried sediment sample was added to 15 ml of distilled water,

129 placed in a shaker, and shaken at a speed of 4000 rpm for 5 minutes. The centrifuged supernatant was

130 then poured out and these steps were repeated 3 times. To remove organic matter, 10 ml of a 15%

131 H_2O_2 solution was added to the sediment and placed in an ultrasonic oscillator for 24 hours. After

132 adding a second 10 ml of H_2O_2 (15%) to confirm the completion of the reaction, the mixture was

133 centrifuged and the supernatant containing the organic matter was removed. The sediment was then

134 washed by adding 30 ml of distilled water, and the supernatant was again removed after centrifugation.

135 This washing step was repeated 3 times to remove residual H_2O_2 in the centrifuge tube. To remove the

carbonates, we added 10 ml of 10% HCl solution to the centrifuge tube and allowed the acid to react with the sediments for 24 hours. An additional 10 ml of HCl was then added to confirm the completeness of the reaction. The sample was then centrifuged, and the supernatant was decanted to remove the carbonates. The sample was then rinsed with 30 ml of distilled water, centrifuged, and decanted. This step was performed 3 times to remove any residual HCl.

To disperse sediment agglomeration, we added 10 ml of 1% $Na(PO_3)_6$ solution to the sediment and let the sample react for more than half a day. The grain size of the sediment samples was obtained by Laser Diffraction Particle Size Analyzer LA950 at the GFZ German Research Centre for Geosciences. By using LA950, we measured grains in the size range of between 100 nm to about 3 cm.

3.4 Calculation of the enriched ratio and sodium adsorption ratio (SAR)

In order to classify the supply of different ion sources during the typhoon event, we used the enriched ratio of concentration as a reference. The enriched ratio is the ion concentration at a certain time divided by the ion concentration at the first observation. A value greater than 1 represents a point in time when the sample is more concentrated relative to the first observation, whereas a value smaller than 1 represents a point in time when the sample is more diluted relative to the first observation. The first observation was sampled 6 hours before the typhoon which represents the background value of river water chemistry in this study.

Dissolved calcium and magnesium can stabilize soil aggregates and therefore enhance water permeability (Nadler et al., 1996). By contrast, excess sodium can disperse soil particles through deflocculation, thereby reducing water permeability (Hanson et al., 1999). The potential for material dispersion in badlands is generally determined by measuring the presence and behavior of sodium and is quantified by the sodium absorption ratio (SAR), (1):

161 $$SAR = \frac{Na^+}{\sqrt{\left(\frac{Ca^{2+}+Mg^{2+}}{2}\right)}}$$ (1)

162 Here, the cation measurements are expressed in milliequivalents per liter (meq/L). For pore water,

163 when SAR is greater than 13, the excess sodium causes soil particles to repel each other, preventing

164 the formation of soil aggregates (Seelig, 2000; Horneck et al., 2007). Given the influence of soil

165 structure, SAR value for irrigation water smaller than 3 is low, from 3 to 9 is medium and above 9 is

166 high (Ayers and Westcot, 1985).

167

168 3.5 Calculation of TDS and chemical weathering rate

169 Riverine TDS is widely used to estimate chemical weathering rates of river catchments (e.g. Gaillardet

170 et al. 1999). In this study, riverine TDS (in units of μmol/L) is expressed as:

171 $TDS = TDS_{rain} + TDS_{evaporite} + TDS_{sil} + TDS_{carb}$ (2)

172 where the contributions from precipitation (TDS_{rain}), evaporite ($TDS_{evaporite}$), silicate weathering

173 (TDS_{sil}) and carbonate weathering (TDS_{carb}) are considered. We calculated the proportions of ion

174 contributions from rainwater, evaporite, silicate and carbonate for Ca, Mg, Na, Cl, and SO_4 with the

175 MEANDIR inversion model (Kemeny and Torres, 2021), a MATLAB script for inverting fractional

176 contributions of end-members, and for constraining the chemical compositions of those end-members

177 with Monte Carlo propagation of uncertainty. To exclude the input of precipitation (TDS_{rain}) from

178 riverine TDS, we used local rainwater Cl^- concentrations with an average value of 68 μmol/L (Lu,

179 2014), and also the ratios of SO_4/Cl, Na/Cl, K/Cl, Mg/Cl, Ca/Cl in rainfall based on the rainfall

180 chemistry from 2007 to 2013 reported by Lu (2014) (Table 1).

181 $[X]_{norain} = [X]_{river} - [X]_{rain}$ (3)

182 $TDS_{rain} = \sum[X]_{rain}$ (4)

183 Here $[X]_{norain}$ reflects the remaining concentration of ion X after the removal of atmospheric inputs;

184 $[X]_{river}$ is the concentration of ion X in river water, and $[X]_{rain}$ is the concentration of ion X from

atmospheric deposition. In the second step, we corrected for evaporite inputs (TDS$_{evaporite}$) using the following equation:

$$[X]_{NSS} = [X]_{norain} - [X]_{evap} = [X]_{norain} - \left([Cl]_{norain} \times (\frac{X}{Cl})_{evap}\right) \tag{5}$$

$$TDS_{evaporite} = \Sigma[X]_{evap} \tag{6}$$

where [X]$_{NSS}$ is the concentration of ion X after the removal of ions attributed to evaporites, [X]$_{evap}$.

[X/Cl]$_{evap}$ is the ratio of ion X and Cl by using the end-member molar ratios of evaporite reported by

Burke et al. (2018), of which K/Cl is referred to Chao et al., (2011) (Table 1)). Then, after the correction

for evaporite, the chemical weathering budget can be divided into contributions by silicate (TDS$_{sil}$)

and carbonate weathering (TDS$_{carb}$), expressed as:

$$TDS_{sil} = [Na]_{sil} + [K]_{sil} + [Mg]_{sil} + [Ca]_{sil} + [SiO_2]_{sil} \tag{7}$$

$$TDS_{carb} = [Mg]_{carb} + [Ca]_{carb} + [HCO_3]_{carb} \tag{8}$$

$$[HCO_3]_{carb} = \frac{1}{2}([Mg]_{crab} + [Ca]_{crab}) \tag{9}$$

where [Na]$_{sil}$ and [K]$_{sil}$ are riverine [Na]$_{NSS}$ and [K]$_{NSS}$ concentrations, respectively. We used endmember values for silicate- and carbonate-dominated rocks reported by Gaillardet et al. (1999) (Table 1). We agree that the use of global endmembers leads to a larger range of estimations, but is still appropriate in discussing trends in weathering rates.

Considering the hydrological response, we use flow weighted method to calculate the flux of solute

(Huang et al., 2012), expressed as:

$$Flux_{(rain,\ evap,\ sil,\ carb)} = \left. \left(m \times \frac{\Sigma_{i=1}^{n} TDS_{(rain,\ evap,\ sil,\ carb)\ i}}{\Sigma_{i=1}^{n} Q_i} \times Q_t\right) \middle/ \text{catchment area} \right. \tag{10}$$

where m is the conversion factor for a specific unit (ton/km^2/yr). Q_i is the hourly discharge corresponding to sampling time. Q_t is total discharge during the year or during the typhoon.

Table 1 Input end-members for the mixing model.

End-member	SO$_4$/Cl	Na/ Cl	K/ Cl	Mg/Cl	Ca/Cl
Precipitation	0.35	0.90	0.09	0.18	0.35
Evaporites	0.6±0.6	1.0±0	0.026	0.1±0.08	0.5±0.5
	Ca/Na	Mg/Na			
Silicates	0.35±0.25	0.24±0.2			
Carbonates	60±30	30±15			

4. Results

4.1 Geochemistry of river water and suspended sediment

In 2017, the Nesat and Haitang typhoons brought 579 mm of rainfall over three days, with a maximum intensity of 74 mm/hr. The discharge at Nanxiong Bridge demonstrated that the climatic co-response has two pulses (Fig. 2). Since the time interval between the two typhoons was less than 6 hours, we define the two typhoons as one typhoon event and distinguish between a first and second discharge pulse. We quantify time relative to the onset of the typhoon (0 hr). The first pulse occurred from 8.5 to 32.5 hr, with a mean water discharge of 66.2 m^3/s. The second pulse that occurred from 32.5 to 62.5 hr had a 5.5 times higher mean discharge of 369.2 m^3/s. The maximum discharge (753.2 m^3/s) was observed during the second pulse at 44.5 hr (July 31st, 2017, at 6:00 a.m.) (Fig. 2).

At Nanxiong Bridge, SSC has a statistically significant positive correlation with SAR ($\rho = 0.51$, $p < 0.05$). SSC has two peaks, one during each pulse, but SAR only shows a peak during the first pulse. During the first pulse, SSC ranged from 10 to 33757 mg/L and SAR increased from 1.44 and to 3.14. During the second pulse, SSC increased from 5445 to 16900 mg/L and SAR remained about 1.44. The median grain size (D$_{50}$) ranged from 3.9 to 8.2 μm, with an average value of 5.6 μm during the second pulse, and exhibited a positive correlation with discharge ($\rho = 0.40$). At Guting Bridge, SSC has a statistically significant positive correlation with SAR ($\rho = 0.69$, $p < 0.05$) during the survey. SSC ranged from 164 to 19538 mg/L before the first pulse and ranged from 2857 to 35920 mg/L during the second pulse, while SAR showed a mean of 1.46 and two peaks with a value over 4 during both pulses.

229 D_{50} ranged from 3.6 to 8.8 μm, with an average value of 5.3 μm during the second pulse, (Fig. 2). In

230 terms of sediment chemistry at Guting Bridge, major elements of the two selected sediment samples

231 show that calcium and sodium accounted for about 10% of the mass loss between the typhoon event

232 (5.5 hr of duration) and the peak of discharge (41.5 hr of duration) (Table. S4).
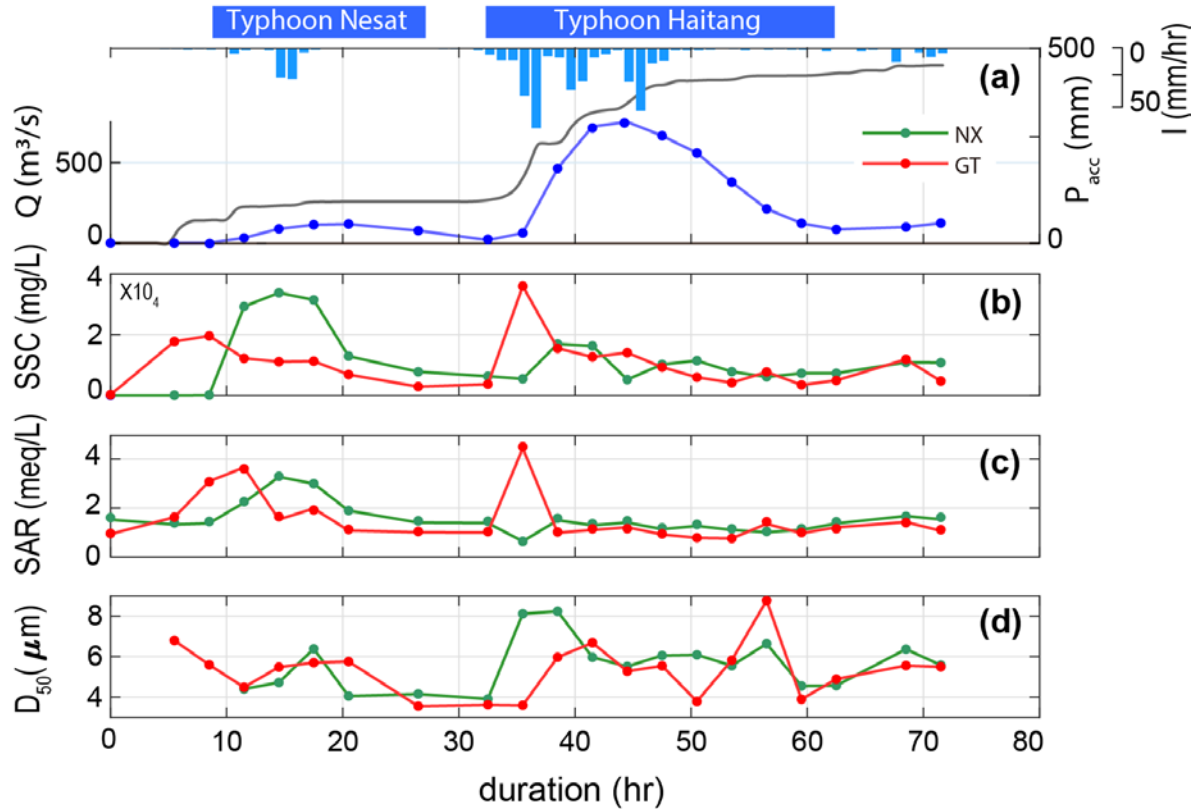
Figure 2. Timeseries SSC, SAR and median grain size of suspended sediment (D_{50}) at two sampling
sites. The blue line denotes hourly discharge (Q) at Nanxiong Bridge, and the blue bar denotes hourly
precipitation (I) at Gutingkeng station. The gray line denotes precipitation accumulation (P_{acc}), the
green line denotes the Nanxiong Bridge (NX) dataset, and the red line denotes the Guting Bridge (GT)
dataset.

240 The fractional proportions of TDS at Nanxiong Bridge during baseflow show that precipitation,

241 evaporites, silicates, and carbonates contribute 3.0±1.1% (uncertainty gives the standard error of the

242 mean), 28.7±14.6%, 26.9±6.5%, and 41.4±13.2%, respectively (Fig. 3a). During the typhoon event,

243 the proportion of TDS at Nanxiong Bridge attributed to TDS_{rain} is 6.3±2.4%. $TDS_{evaporite}$ contributes

244 32.4±13.6% and increases from 27.4% to 61.1% at the incipient first pulse. TDS_{sil} contributes

245 39.5±15.2%, which is 12.6% higher than the non-typhoon period. TDS_{carb} contributes 21.8±11.5 %

246   (Fig. 3b), which is 19.6% lower than the non-typhoon period. The fractional proportions of TDS at the

247   Guting Bridge show that $6.5\pm2.1\%$ of TDS is contributed by TDS_{rain}. $TDS_{evaporite}$ contributes

248    $24.8\pm16.2\%$ and increases from 13.6% to 61.6% at the incipient second pulse, when the SSC and SAR

249   peak simultaneously. TDS_{sil} and TDS_{carb} contribute $39.5\pm15.2\%$ and $27.5\pm16.7\%$, respectively (Fig.

250   3c).

251

252   Enriched ratios of less than one indicate dilution, and values greater than one indicate concentration.

253   Since we set the ion concentration of rainfall to be constant during the typhoon event, the enriched

254   ratio of precipitation is constant throughout the observation period. At Nanxiong Bridge, the evaporites

255   enriched ratio increases from 0.4 to 1.7 between the two pulses and decreases to 0.1 at the discharge

256   peak. The silicates enriched ratio increases from 1 to 1.5 before the first pulse and decreases to 0.1 at

257   the peak of discharge, then returns to 1 before the observation ends. The concentration attributed to

258   carbonates is always diluted. The evaporites and carbonates enriched ratio has a statistically significant

259   negative correlation with discharge (evaporites: $\rho = -0.67$, carbonates: -0.60, $p<0.05$) and the silicate

260   enriched ratio has a negative correlation with discharge ($\rho = -0.32$), indicating dilution by typhoon

261   rainfall (Fig. 3d). At Guting Bridge, the evaporites enriched ratio has two peaks during the two pulses

262   with a value of 5.2 at the first peak, a value of 4.7 at the second peak. After the event, the value returns

263   to about 1.2. Notably, the evaporites enriched ratios during both pulses are similar, but the peak

264   discharge of the second pulse is 5.5 times higher than that of the first pulse. The silicate enriched ratio

265   has an analogous pattern with the evaporites enriched ratio, but the enriched ratio is smaller. Similar

266   to Nanxiong Bridge, the carbonates enriched ratio is always diluted at Guting Bridge (Fig. 3e). The

267   evaporite and silicate enriched ratio shows a statistically significant positive correlation ($\rho = 0.96$,

268    $p<0.05$), and the evaporite and silicate enriched ratios have a statistically significant positive

269   correlation with SAR ($\rho = 0.86$, $\rho = 0.84$, $p<0.05$). We also use the concentration–discharge (cQ)

270   relationship of each ion at rising and recession limb, as well as baseflow at Nanxiong Bridge to assess

271   the state of dilution behavior (Fig. S2). Overall, our results show that all ions are in a dilution, and the

272   dilution in recession limb is stronger than that in rising limb, except for SO_4 during baseflow (θ=0.07).

273   The concentration of Na, Cl and K during baseflow have a higher variability than the values during

274   the event. Additionally, Na, Cl, and SO_4 increase the concentration with increasing flow at the certain

275   period of rising limb.
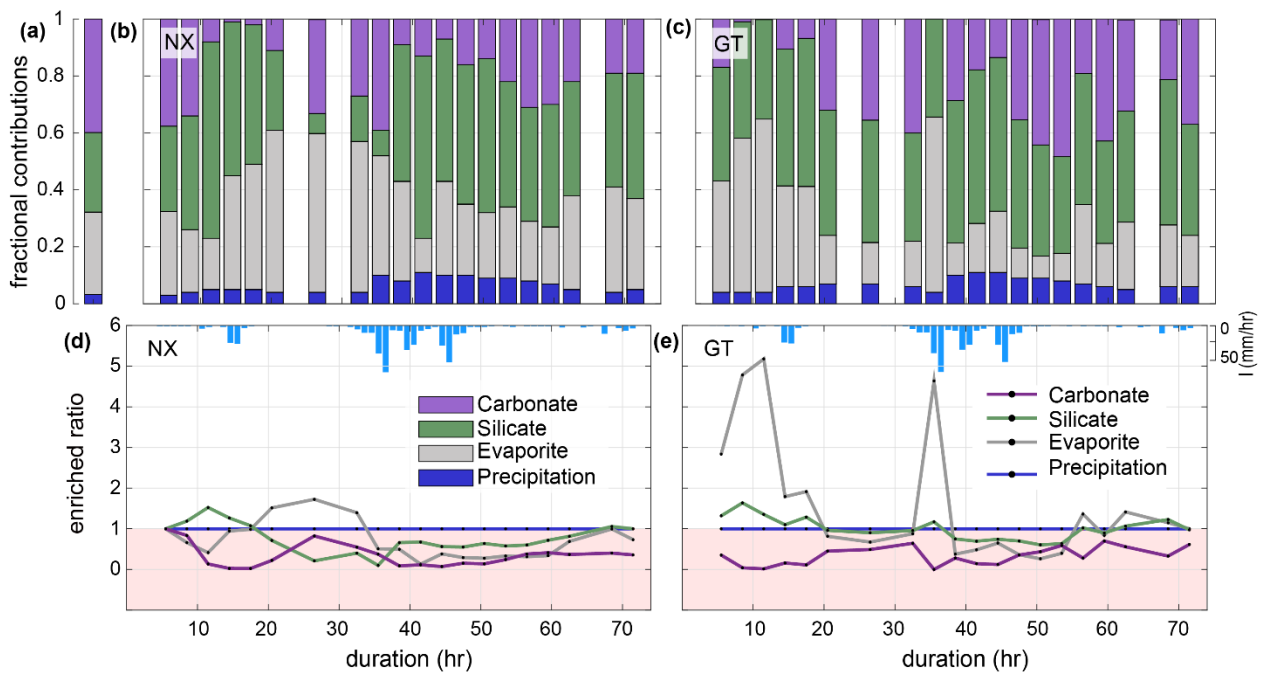
Figure 3. Timeseries illustrating TDS sources during the typhoon event at the two sampling sites. Fig.3a shows the average proportion of TDS for the non-typhoon period from September 2014 to December 2016 at Nanxiong Bridge; Fig.3b-c denotes the endmember contributions to TDS at Nanxiong Bridge dataset and Guting Bridge dataset from the typhoon period; the purple bar denotes TDS_{carb} (Eq. 8); green denotes TDS_{sil} (Eq. 7); the gray bar denotes $TDS_{evaporite}$ (Eq. 6); the blue bar denotes TDS_{rain} (Eq. 4). Fig.3d-e denotes the enriched ratio of ion concentrations by TDS sources from the Nanxiong Bridge dataset and Guting Bridge dataset during the typhoon period. The purple line denotes TDS_{carb}, the green line denotes TDS_{sil}, the gray line denotes $TDS_{evaporite}$, the blue line denotes the TDS_{rain}, and blue bar denotes hourly precipitation (I) at GTK station.

4.2 Evaporite, silicate and carbonate dissolution over time

287

288   We calculated the enriched ratios of ions (i.e., Na^+, Cl^-, Ca^{2+} and SO_4^{2-}) that are sourced from evaporites

289   (i.e., halite (NaCl) and gypsum ($CaSO_4$)). The variability in the concentrations of each of these ions

290   reflects the overall trends in TDS (Fig. 3d-e & Fig. 4).

291

292   At Nanxiong Bridge, all evaporite and carbonate ions have a statistically significant negative

293   correlation with discharge. The enriched ratios in evaporite Na^+, Cl^- and SO_4^{2-} have the same trend (Fig.

294   4), which show an initial decrease during the first pulse, followed by an increase to 2 between the two

295   pulses, and a final decrease during the second pulse. Evaporite Ca^{2+} shows a similar trend with

296   evaporite Na^+, Cl^- and SO_4^{2-}, but the values are below 1. The enriched ratios of silicate Na^+, Ca^{2+} show

297   an increase during the first pulse and a decrease to less than 1 before the rainfall peak, followed by an

298   increase from about 0.06 to 1.11 at the end of observation. At Guting Bridge, all evaporite ions have a

299   statistically significant positive correlation with the corresponding silicate ions (Na^+, $\rho = 0.98$; Ca^+, ρ

300   $= 0.81$, $p<0.05$). Evaporite Na^+, Cl^-, and SO_4^{2-} each have two peaks that occur prior to the maximum

301   rainfall and reflect a factor of 5 increase in the enriched ratio. Compared with Nanxiong Bridge

302   (downstream), the enriched ratio in evaporite Ca^{2+} at Guting Bridge concentrates at the onset of the

303   first pulse and after peak discharge. Additionally, the enriched ratios of carbonate at Guting Bridge are

304   similar to Nanxiong Bridge, and are always below 1.
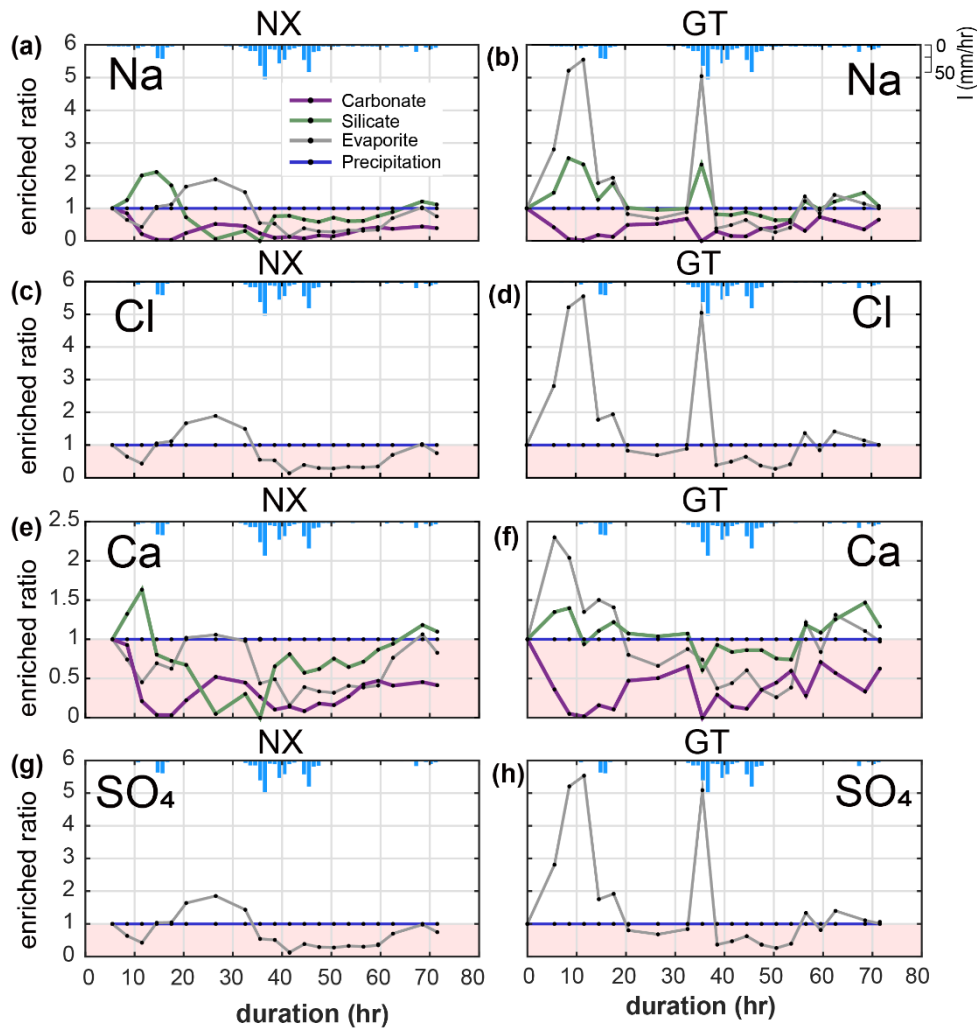
Figure 4. Time-series patterns in enriched ratio at two sampling sites. NX denotes the Nanxiong Bridge dataset and GT denotes Guting Bridge dataset. The pink area indicates enriched values below 1. Blue bar denotes hourly precipitation (I) at Gutingkeng station.

Gaillardet et al. (1999) documented that dissolved ions ratios of Ca/Sr and Na/Sr are distinct for carbonates (low Na/Sr, high Ca/Na) versus silicates or evaporites (high Na/Sr, low Ca/Na). We use these ratios to elucidate potential mixing between carbonates, silicates, and evaporite endmenbers (Fig. 5). At Nanxiong Bridge, non-typhoon ratios of Na/(1000*Sr) and Ca/(1000*Sr) are 0.23–0.68 and 0.19–0.35, respectively (Table S4). These values increase markedly during the typhoon events, with enriched– ratios of Na^+ exceeding 5 at T = 11.5 and 35.5 hr. The high concentration of Na^+, Cl^- and SO_4^{2-} (as illustrated in the enriched ratio) indicate that there is enhanced dissolution of evaporites at the onset of the typhoon event, especially at Guting Bridge. Subsequently, the concentration of Na^+

decreased with sustained rainfall. Then, the ratios approach the silicates/carbonates weathering (high

Na/Sr, high Ca/Sr ratios) after the peak discharge.
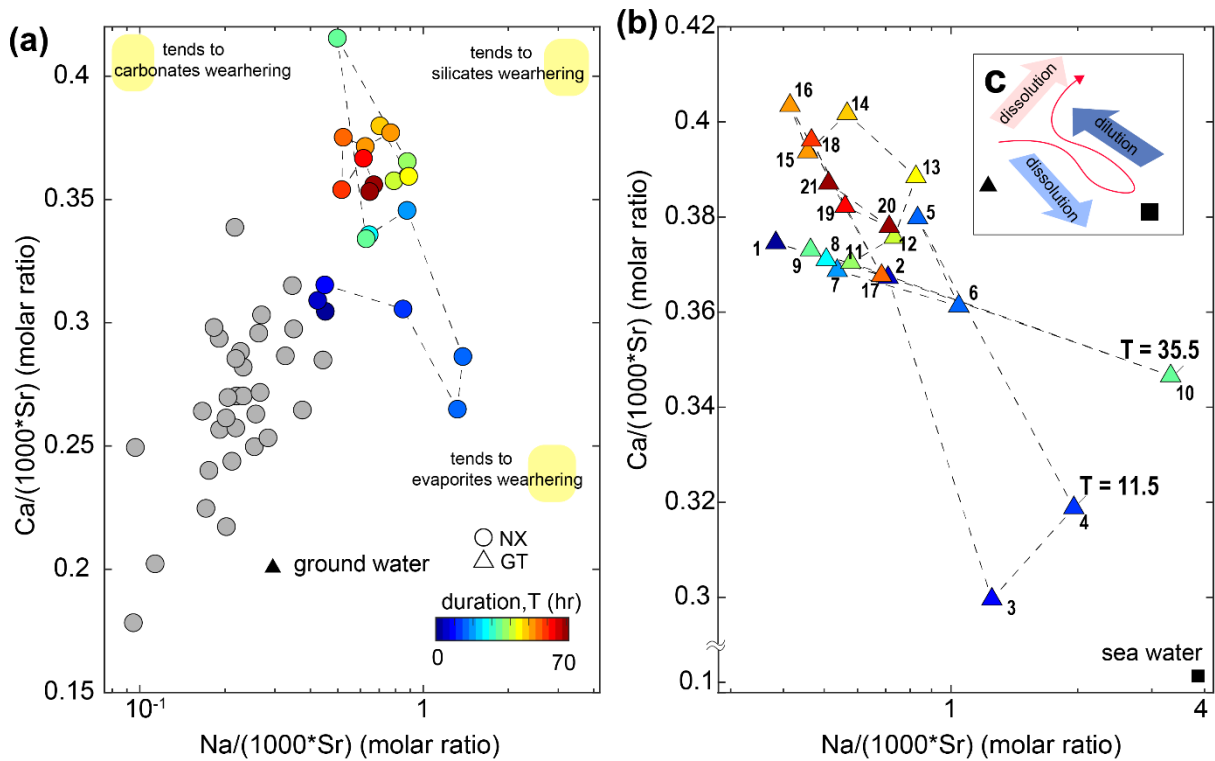
Figure 5. Molar ratio mixing diagrams of Erren River waters for (a-b) Na/(1000*Sr) versus Ca/(1000*Sr), circles denote dataset at Nanxiong Bridge, and triangles denote dataset at Guting Bridge. Colorbar denotes survey duration. Gray circles denote the dataset at Nanxiong Bridge during baseflow conditions from 2014 to 2016. The black triangle illustrates the groundwater endmember (Chao et al., 2011); the black square illustrates the seawater endmember. Numbers in the triangle represent the time sequence, 1 represents the start point, and 21 represents the end point. Yellow areas indicate trends in weathering types rather than the locations of endmember. (c) Illustration of dynamic weathering. The red line indicates the direction of change with time. The light blue arrow denotes dissolution of evaporite, the dark blue arrow denotes dilution from rainfall, and the red arrow denotes dissolution of suspended sediment.

5. Discussion

5.1 Relationships between dissolved evaporite and river water chemistry

Before the survey, the monthly rainfall of the study area was 72.5 mm, which is only 18% of the

average monthly rainfall, implying that it provides a relatively dry environment for accumulating
evaporites on the slope surface. Under maximum rainfall intensity, Na^+, Cl^- and SO_4^{2+} at Guting Bridge
show markedly increased concentrations at the onset of the typhoon, peaks in enriched ratios that
exceed 5 (Fig. 4), and the greatest contribution of dissolved ions from evaporites (Fig. 3). Calculated
with pore water chemistry during the dry season from the same study site, the sodium absorptions ratio
(SAR) is 240.8 and exceeds the threshold value of 13. During the typhoon event, the river water SAR
has a maximum value of 4.41 at Guting Bridge (3.14 at Nanxiong Bridge), suggesting soil
deflocculation within river is weaker than on the hillslopes. However, the SAR has a statistically
significant positive correlation with $TDS_{evaporite}$ ($\rho = 0.86$, $p<0.05$) at Guteng Bridge (upstream). This
pattern indicates that excess sodium is effective at inducing material dispersion at hillslopes and thus,
contributing to a higher suspended sediment load. The trend of river water SAR is able to reflect the
extent of dissolved Na^+ from hillslope. (Fig. 2).

These observations and results suggest that rainwater in the typhoon event rapidly dissolves the
evaporites on the slope surface, which produces high measured concentrations of Na^+, Cl^-, and SO_4^{2+}
during the time of peak precipitation (30-40 hr of duration). Furthermore, the dissolution of the near-
surface evaporite deposits should be most heavily influenced by runoff from the hillslopes, so we
expect that excess sodium and enhanced erosion will be most significant on the hillslopes.

At Nanxiong Bridge, we observe a 10-hour delay in the peak enriched ratio relative to the SAR (Fig.
3d) and overall lower enriched ratios relative to Guteng Bridge (Fig. 3d-e). We suggest that dilution
and the transport distance from the badlands are responsible for this. The two catchments have a similar
areal extent of badlands within the total catchment area, which is about 2.49% at Nanxiong Bridge
catchment and 2.37 % in Guting Bridge catchment. Badlands contribute considerable evaporite solutes
(Chou, 2008), but the higher downstream drainage area will result in dilution of the solutes without
additional inputs. Additionally, Nakata and Chigira (2009) have observed that salt dissolution induces

362 an increase in electrical conductivity during intermittent rainfall events and decreases gradually after

363 rainfall events when evaporation and salt precipitate. Therefore, re-crystalization during the

364 transportation is to be expected.

365

5.2 From evaporite dissolution to silicate weathering

367 Our observations show that silicate weathering during the typhoon event contributes 16.8 ton/km^2/yr,

368 corresponding to 16.6% of the annual silicate weathering flux (Table S3). Additionally, we observed a

369 change in dominant chemical weathering mechanism during the typhoon event. We rule out significant

370 contributions from groundwater and deep seawater after peak discharge, since ratios shift to higher

371 Na/Sr, and Ca/Sr ratios relative to the non-typhoon ratio (Fig. 5a–b), and the Ca/Sr ratio of mud

372 volcanoes in the study site is one order of magnitude less than river water (Chao et al., 2011). Carbonate

373 weathering is the primary contributor of Ca^{2+} for most of the world's large rivers (Gaillardet et al.

374 1999), but the increased Na^+ and consistently enriched ratio of carbonate Ca^{2+} does not make this a

375 likely main contributor to the Erren River during the typhoon. We thus suggest that the primary

376 contributor to weathering is enhanced silicate dissolution. This interpretation is supported by the

377 temporal evolution of the enriched ratio of silicate Ca^{2+}, which gradually increases after the discharge

378 peak, to approach a value of about 1 at the end of survey (Fig. 4e&f). As such, in the waning of the

379 event, excess Ca^{2+} originates from a silicate source. Therefore, we suggest that the ratios shift to higher

380 Na/Sr, Ca/Sr ratios due to enhanced silicate weathering during the typhoon. We also observe that the

381 masses of Na and Ca are reduced by 10.6% and 9.9%, respectively, in the suspended sediment during

382 the course of the typhoon event (Table S6).

383

384 Given that the sediment transported in the channel is supplied by physical erosion, we suggest that

385 physical erosion in our study site enhances silicate chemical weathering, which is consistent with

386 previous studies (Chung, 2002; Chou, 2008). Moreover, we associate the change in weathering regime

during the course of the typhoon with abrasive erosion of silicate sediments in the channel. Mechano-chemical dissolution of weakly bound ions, e.g., F^- from the fresh muscovite surfaces is driven by abrasion under high energy sediment transport with reorganization of the river bed (Andermann et al., 2022). Mudstones are mainly composed of silicate minerals (e.g., illite and chlorite minerals) (Tsai, 1984a), and a few swelling clay minerals (e.g., montmorillonite), which provide an abundant silicate pool. We suggest that high suspended sediment concentrations, combined with high energy flow during the typhoon, caused increased silicate input from the weathered silicates in the suspended sediment. This trend can explain about 10% of the reduced mass and it has also been observed in typhoon-driven silicate chemical weathering from silicate minerals at surface (Meyer et. al., 2017). Importantly, the global annual silicate weathering flux of rivers is 15.7 ton/km^2/yr (Gaillardet et al. 1999), relative to our value of 16.8 ton/km^2/yr., suggesting that individual stochastic events may have global relevance.

5.3 Typhoon-controlled cycles of physical and chemical erosion

Evaporites, including halite (NaCl) and gypsum (CaSO$_4$), are found in few sedimentary environments, and they are often excluded from the estimation of CO$_2$ consumption   (Gaillardet et al., 1999). Compared to silicate rocks, the relation between evaporites weathering and physical erosion has rarely been discussed. Through the interactions among riverine chemistry, suspended sediment properties, and previous soil water chemistry studies, we suggest a positive feedback cycle of physical-chemical erosion driven by mobile dissolved evaporite (Fig. 5). The feedback cycle includes three steps. (1) precipitation and deposition of evaporite during the dry season in near-surface mudstone desiccation cracks through capillary transport (Higuchi et al., 2013, 2015; Nakata and Chigira, 2009). In the dry season, exposed bedrock with low water content develops desiccation cracks (Allen, 1982; Goehring et al., 2010; Kindle, 1917; Seghir and Arscott, 2015; Xiaa and Hutchinson, 2000), providing space for the re-precipitation of evaporite minerals. Using evidence from core samples in mudstone bedrock at the study site, the depth of the crack of about 20 cm can be regarded as the thickness of the weathering layer. Higuchi et al. (2013) suggested that the weathering layer in the top 10 cm of mudstone can easily

413 be eroded by intense rainfall. Erosion exposes fresh bedrock, which would dry in the following dry

414 season and further produce weatherable material.

415

416 (2) Rainfall dissolves the evaporites, producing sodic water that increases physical erosion during

417 typhoon events. The resulting dissolved sodium causes higher hillslope erosion by deflocculation,

418 leading to increased suspended sediment in the channels. In the study site, hillslope erosion rate is

419 about 9-30 cm/year (Higuchi et al., 2013; Yang et al., 2021a). At Nanxiong Bridge, the denudation rate

420 approaches about 142,857 ton/km^2/yr, measured from river suspended load (Dadson et. al., 2003), and

421 the chemical weathering flux is 124-237 ton/km^2/yr (Chou, 2008; this study). The high hillslope

422 erosion rate ensures a steady supply of freshly exposed bedrock, allowing for high chemical weathering

423 rates.

424

425 (3) Physical erosion enhances silicate weathering and bedrock exposure on hillslopes. Clay minerals

426 in mudstone deposits are abraded from the abundantly available sediment and provide material for

427 silicate weathering in streams. Ultimately, with frequent typhoon events and high temperatures in the

428 study area, this dynamic cycle could repeat several times a year.

429
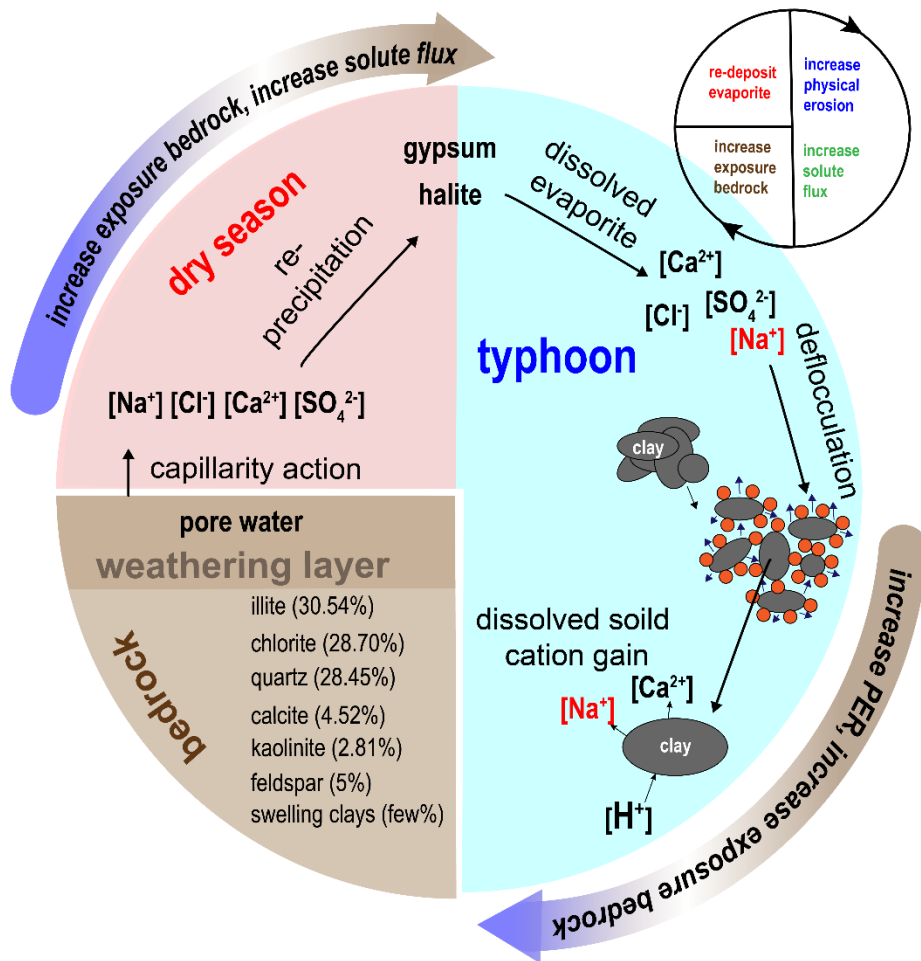
Figure. 6. Cycle of feedback between physical erosion rate (PER) and solute flux in badlands catchment. Red blocks represent dry season conditions. Blue region represents typhoon conditions. Brown region represents the bedrock and indicates the type and proportion of minerals of mudstone (Tsai, 1984b).

6. Conclusion

We presented major element compositions of stream water from two sites in the Erren River catchment at three-hour intervals during a three-day typhoon event in 2017. At Guteng Station (upstream), $TDS_{evaporite}$ is covariant with TDS_{sil}, the sodium adsorption ratio, and the suspended sediment concentration, which can be assigned to dissolved evaporite (e.g., halite and gypsum). The excess sodium in the evaporite deposits causes material dispersion through deflocculation, which enhances the suspended sediment flux. Our observations show that the water chemistry of the typhoon event is mainly contributed by silicate weathering at 16.8 ton/km^2/yr and evaporite weathering at 10.9

443 ton/km^2/yr, in contrast with baseflow (non-typhoon) conditions that are mainly contributed by

444 carbonate weathering. Moreover, during the course of the typhoon, we observed a shift from

445 predominantly evaporite weathering during peak precipitation to silicate weathering at peak discharge.

446

447 Combining the observation of riverine chemistry, suspended sediment properties, and previous soil

448 water chemistry studies, we propose a feedback cycle between physical erosion and chemical

449 weathering in badlands topography, illustrating that precipitation of evaporites during the dry season

450 produces sodic water during typhoon events and preferentially triggers higher local erosion. The

451 enhanced hillslope erosion and abrasive effects of clay in a high discharge stream enhance bedrock

452 exposure on hillslopes and silicate weathering, respectively. Newly exposed bedrock then produces

453 more weathered material. Although measurements of bedrock mineral chemistry and Sr isotope are

454 still needed for confirming sources of excess sodium and calcium (Fig. 5), we suggest that the

455 conceptual model could provide an insight into landscape change of badlands. The results from our

456 study suggest that high erosion rates in mudstone badlands of the Erren River catchment are due to

457 both weakened lithology and the interaction between evaporites and hillslope erosion.

458

459 *Data availability.* Relevant data supporting the findings of the study are available in the Supplementary

460 Information, or from the corresponding author upon request. Source data are provided with this paper.

461

462 *Author contributions.* C.-J.Y. designed the study and conducted field surveys, data analysis, and

463 modelling. P.-H. C. conducted data analysis. S. X. conducted modelling. T. Y. T. provided the verified

464 data. J.-C.L. and J.-C. Huang contributed to the scientific discussion, interpretation.C.-J.Y., E. D. E.

465 and J.M.T. wrote the paper with input of all authors.

466

467 *Competing interests.* The authors declare that they have no competing interests.

468

Acknowledgements. We express our gratitude to Niels Hovius for fruitful discussions that greatly improved this work. Special thanks are also given to Sheng-Wei Guo, Meng-Chang Lu for field work. This is study was supported by grants from National Science and Technology Council, Taiwan to Ci-Jian Yang (MOST 110-2917-I-564-009-).

References

1. Allen, J.R.L.: Sedimentary structures: Their Character and Physical Basis. Developments in sedimentology. 30B, II. Elsevier, Amsterdam. 1982.

2. Andermann, C., Galy, A., Hennig, S., Zimmermann, B., Tipper, E. T., Erlanger, E., Cook, K. L., Schleicher, A., Benning, L., and Hovius, N.: Erosion and weathering forensics of a catastrophic glacial lake outburst flood in Nepal, EGU General Assembly 2022, Vienna, Austria, 23–27 May 2022, EGU22-10417, https://doi.org/10.5194/egusphere-egu22-10417, 2022.

3. Ayers, R., Westcot, D.: Water quality for agriculture. FAO Irrigation and drainage paper 29, 1985.

4. Burke, A., Present, T., Paris, G. Rae, Emily C.M., Sandilands, B. Gaillarde, J., Peucker-Ehrenbrink, B., Fischer, W. W., McClelland, J. W., Spencer, R. G. M., Voss, B. M., Adkins, J. F.: Sulfur isotopes in rivers: Insights into global weathering budgets, pyrite oxidation, and the modern sulfur cycle. Earth and Planetary Science Letters, 496. https://doi.org/10.1016/j.epsl.2018.05.022, 2018

5. Calmels, D., Galy, A., Hovius, N., Bickle, M. J., West, A. J., Chen, M.-C., Chapman, H.: Contribution of deep groundwater to the weathering budget in a rapidly eroding mountain belt, Taiwan. Earth and Planetary Science Letters, 303 (1-2), 48–58. https://doi.org/10.1016/j.epsl.2010.12.032, 2011

6. Carey, A. E., Gardner, C. B., Goldsmith, S. T., Lyons, W. B., Hicks, D. M.: Organic carbon yields from small, mountainous rivers, New Zealand. Geophysical Research Letters, 32, 15404. https://doi.org/0.1029/2005GL023159, 2005.

7. Chao, H.-C., You, C.-F., Wang, B.-S., Chung, C.-H., Huang, K.-F.: Boron isotopic composition of

495 mud volcano fluids: Implications for fluid migration in shallow subduction zones. Earth and

496 Planetary Science Letters, 305. https://doi.org/10.1016/j.epsl.2011.02.033, 2011.

497 8. Cheng, Y.-C., Yang, C.-J., Lin, J.-C.: Application for Terrestrial LiDAR on Mudstone Erosion

498 Caused by Typhoons. Remote sensing, 11(20), 2425. https://doi.org/10.3390/rs11202425, 2019.

499 9. Chou, C.-L.: Sediment Weathering and River Water Chemistry in the Erren Drainage Basin,

500 Southern Taiwan. Master thesis of Department of Earth Sciences, National Cheng Kung

501 University, 1–103, 2008.

502 10. Chung, S.-L.: Preliminary Geochemical and Isotopes study of the Erren river water. Master thesis

503 of Department of Earth Sciences, National Cheng Kung University, 1–95, 2002.

504 11. Clift, P. D., Wan, S., Blusztajn, J.: Reconstructing chemical weathering, physical erosion and

505 monsoon intensity since 25Ma in the northern South China Sea: A review of competing proxies.

506 Earth-Science Reviews, 130, 86–102. https://doi.org/10.1016/j.earscirev.2014.01.002, 2014.

507 12. Dadson, S. J., Hovius, N., Chen, H., Dade, W. B., Hsieh, M.-L., Willett, S. D., Hu, J.-C., Horng,

508 M.-J., Chen, M.-C., Stark, C. P., Lague, D. Lin, J.-C.: Links between erosion, runoff variability

509 and seismicity in the Taiwan orogen. Nature, 426(6967), 648–651,

510 https://doi.org/10.1038/nature02150, 2003.

511 13. Emberson, R., Hovius, N., Galy, A., Marc, O.: Chemical weathering in active mountain belts

512 controlled by stochastic bedrock landsliding. Nature Geoscience, 9, 42–47.

513 https://doi.org/10.1038/ngeo2600, 2016.

514 14. Faulkner, H., Alexander, R., Teeuw, R., Zukowskyj, P.: Variations in soil dispersivity across a

515 gully head displaying shallow sub-surface pipes, and the role of shallow pipes in rill initiation.

516 Earth Surface Process and Landforms. 29, 1143–1160. https://doi.org/10.1002/esp.1109, 2004.

517 15. Gaillardet, J., Dupre, B., Louvat, P., Allegre, C. J.: Global silicate weathering and CO_2

518 consumption rates deduced from the chemistry of large rivers. Chemical Geology, 159, 3–30.

519 https://doi.org/10.1016/S0009-2541(99)00031-5, 1999.

520 16. Goehring, L., Conroy, R., Akhter, A., Cleggb, W.J., Routh, A.F.: Evolution of mud-crack patterns

521   during repeated drying cycles. Soft Matter, 6, 3562–3567. https://doi.org/10.1039/B922206E,

522   2010.

523   17. Hanson, B., Grattan, SR., Fulton, A.: Agricultural salinity and drainage. University of California

524   Irrigation Program, Davis., 1999.

525   18. Hartshorn, K., Hovius, N., Dade, W. B. Slingerland, R. L.: Climate-Driven Bedrock Incision in

526   an Active Mountain Belt. Science, 297, 2036–2038. https://10.1126/science.1075078, 2002.

527   19. Higuchi, K., Chigira, M., Lee, D.-H.: High rates of erosion and rapid weathering in a Plio-

528   Pleistocene mudstone badland, Taiwan. Catena, 106, 68–82.

529   https://doi.org/10.1016/j.catena.2012.11.005, 2013.

530   20. Higuchi, K., Chigira, M., Lee, D-H., Wu, J-H.: Rapid weathering and erosion of mudstone

531   induced by saltwater migration near a slope surface. Journal of Hydrologic Engineering, 20(6),

532   C6014004. https://doi.org/10.1061/(ASCE)HE.1943-5584.0001105, 2015.

533   21. Horneck, D.S., Ellsworth, J.W., Hopkins, B.G., Sullivan, D.M., Stevens, R.G.: Managing Salt-

534   Affected Soils for Crop Production. PNW 601-E. Oregon State University, University of Idaho,

535   Washington State University, 2007.

536   22. Huang, J.C., Lee, T.Y., Kao, S.J., Hsu, S.C., Lin, H.J., Peng, T.R.: Land use effect and

537   hydrological control on nitrate yield in subtropical mountainous watersheds. Hydrology and

538   Earth System Science, 16(3), 699-714. https://doi.org/10.5194/hess-16-699-2012, 2012.

539   23. Kemeny, P. C., Torres, M. A.: Presentation and applications of mixing elements and dissolved

540   isotopes in rivers (MEANDIR), a customizable MATLAB model for Monte Carlo inversion of

541   dissolved river chemistry. American Journal of Science, 321(5), 579–642.

542   https://doi.org/10.2475/05.2021.03, 2021.

543   24. Kindle, E.M.: Some factors affecting the development of mud-cracks. The Journal of Geology,

544   25(2), 135–144. https://doi.org/10.1086/622446, 1917.

545   25. Knapp, J. L., von Freyberg, J., Studer, B., Kiewiet, L., & Kirchner, J. W.: Concentration–

546   discharge relationships vary among hydrological events, reflecting differences in event

547   characteristics. Hydrology and Earth System Sciences, 24(5), 2561-2576.

548   https://doi.org/10.5194/hess-24-2561-2020, 2020.

549   26. Lee, D.-H., Lin, H.-M., Wu, J.-H.: The basic properties of mudstone slopes in southwestern

550   Taiwan. Journal of GeoEngineering, 2(3), 81–95. https://doi.org/10.6310/jog.2007.2(3).1, 2007.

551   27. Lee, Y.-J., Chen, P.-H., Lee, T.-Y., Shih, Y.-T., Huang, J.-C.: Temporal variation of chemical

552   weathering rate, source shifting and relationship with physical erosion in small mountainous

553   rivers, Taiwan, Catena, 190. https://doi.org/10.1016/j.catena.2020.104516, 2020.

554   28. Lu, S.-C. and Lin, N.-H.: Monitoring and component analysis of acid rain research

555   project. Environmental Protection Agency, Taiwan, 2014.

556   29. Lyons, W. B., Carey, A. E., Hicks, D. M., Nezat, C. A.: Chemical weathering in high-sediment-

557   yielding watersheds, New Zealand. Journal of Geophysical Research-Earth Surface, 110, 11.

558   https://doi.org/10.1029/2003JF000088, 2005.

559   30. Maher, K., and Chamberiain, C. P.: Hydrological Regulation of Chemical Weathering and the

560   Geologic Carbon Cycle. Science, 343, 1502–1504. https://doi.org/10.1126/science.1250770,

561   2014.

562   31. Meyer, K. J., Carey, A. E., You, C.-F.: Typhoon impacts on chemical weathering source

563   provenance of a High Standing Island watershed, Taiwan. Geochimica et Cosmochimica Acta,

564   215, 404–420. https://doi.org/10.1016/j.gca.2017.07.015, 2017.

565   32. Mitchell, J. K.: Volume change behavior. In: Mitchell, J.K., Soga, K. (Eds.), Fundamentals of

566   Soil Behavior. Wiley, 293–333, 1993.

567   33. Moon, S., Huh, Y., Qin, J.H., van Pho, N.: Chemical weathering in the Hong (Red) River basin:

568   Rates of silicate weathering and their controlling factors. Geochimica et Cosmochimica Acta, 71,

569   1411–1430. https://doi.org/10.1016/j.gca.2006.12.004, 2007.

570   34. Nadler, A., Levy, G. J., Keren, R., Eisenberg, H.: Sodic Calcareous Soil Reclamation as Affected

571   by Water Chemical Composition and Flow Rate. Soil Science Society of America Journal. 60 (1):

572   252. Bibcode:1996SSASJ.60.252N. https://doi:10.2136/sssaj1996.03615995006000010038x,

573   1996.

574 35. Nakata, E., Chigira, M.: Geochemistry of erosion processes on badland slopes. A case study of

575   the Gutingkeng formation where mud volcanoes are distributed in southern Taiwan. Journal of

576   Geography, 118(3), 511–532, 2009.

577 36. Negrel, P., Allegre, C.J., Dupre, B., Lewin, E.: Erosion sources determined by inversion of major

578   and trace element ratios and strontium isotopic ratios in river water: The Congo Basin case. Earth

579   and Planetary Science Letters, 120, 59–76. https://doi.org/10.1016/0012-821X(93)90023-3, 1993.

580 37. Rengasamy, P., Greene, R.S.B., Ford, G.W., Mehanni, A.H.: Identification of dispersive behavior

581   and the management of red-brown earths. Australian Journal of Soil Research, 22, 413–443.

582   https://doi.org/10.1071/SR9840413, 1984.

583 38. Rengasamy, P., Olsson, K. A.: Sodicity and soil structure. *Australian Journal of Soil Research*,

584   29, 935–952. https://doi.org/10.1071/SR9910935, 1991.

585 39. Seelig, B. D.: Salinity and Sodicity in North Dakota Soils. EB-57. North Dakota State University,

586   Fargo, ND, 2000.

587 40. Seghir, R., Arscott, S.: Controlled mud-crack patterning and self-organized cracking of

588   polydimeth. Scientific Report, 5, 14787. https://doi.org/10.1038/srep14787, 2015.

589 41. Sherard, J. L., Dunnigan, L. P., Decker, R. S., Steele, E. F.: Identification and nature of dispersive

590   soils. Journal of the Geotechnical Engineering Division, 102, 287–301. 1976.

591 42. Tsai, J. S.: The study on basic properties of mudstone and stabilization methods for   mudstone

592   cut slope in southwestern Taiwan. Master Thesis of Civil Engineering Department, National

593   Cheng Kung University, Tainan, Taiwan, 1984b.

594 43. Xia, Z. C., Hutchinson, J. W.: Crack patterns in thin flms. Journal of the Mechanics and Physics

595   of Solids, 48, 1107–1131. https://doi.org/10.1016/S0022-5096(99)00081-2, 2000.

596 44. Yang, C.-J., Turowski, J. M. Hovius, N., Lin, J.-C., Chang. K.-J.: Badland landscape response to

597   individual geomorphic events. Nature Communications, 12(1):4631.

598   https://doi.org/10.1038/s41467-021-24903-1, 2021a.

599 45. Yang, C.-J., Jen, C.-H., Cheng, Y.-C., Lin, J.-C.: Quantification of mudcracks-driven erosion

600   using terrestrial laser scanning in laboratory runoff experiment. Geomorphology, 375.

601   https://doi.org/10.1016/j.geomorph.2020.107527, 2021b.

602   46. Yang, C.-J., Yeh, L.-W., Cheng, Y.-C., Jen, C.-H., Lin, J.-C.: Badland Erosion and Its

603   Morphometric Features in the Tropical Monsoon Area. Remote sensing, 11(24), 3051.

604   https://doi.org/10.3390/rs11243051, 2019.